THE ROLE OF RARE EARTH DOPANTS IN SEMICONDUCTING HOST SYSTEMS FOR SPIN ELECTRONICS DEVICES

by

Juan A. Colón Santana

A DISSERTATION

Presented to the Faculty of

The Graduate College at the University of Nebraska

In Partial Fulfillment of Requirements

For the Degree of Doctor of Philosophy

Major: Engineering

(Electrical Engineering)

Under the Supervision of Professor Jerry L. Hudgins

Lincoln, Nebraska

July, 2012

The Role of Rare Earth Dopants in Semiconducting Host System for Spin Electronic Devices

Juan A. Colón Santana, Ph.D.

University of Nebraska, 2012

Adviser: Jerry L. Hudgins

The doping of a wide band gap insulator offers an opportunity to increase the coupling between free carriers and magnetic impurities under the magnetic polaron model, leading to an enhanced in the Curie temperature of the host compound, critical for the fabrication of devices with magnetic properties. Some rare earth elements have large intrinsic magnetic moments due to unfilled 4d orbitals, and have been readily incorporated in materials for optical applications. Here the rare earths gadolinium and cerium were explored either as dopants or as part of the high-K semiconducting compound for the fabrication of magnetic heterojunction devices with magnetic properties.

This thesis work explores the effects of rare earth gadolinium and cerium as dopants in high-K compounds such as EuO, HfO_2 and Gd_2O_3. The thesis begins with an exemplary tale of a local moment wide band gap system (although not rare earth based), and a success in achieving negative magneto-resistance in a heterojunction structure with chromium-doped hydrogenated diamond-like carbon (Cr-DLC). In the quest for similar results, we explored the rare earth compounds by means of their electronic band structure using photoemission spectroscopy (PES) and inverse photoemission spectroscopy (IPES) to provide insight into the material functionality and applicability as an electronic device. Rectifying (diode-like) properties were observed in all the heterostructure and each heterojunction device exhibited unique properties that make them suitable for different

applications such as neutron detection or spin electronics applications. Remarkable results were observed on the EuO compound with the inclusion of 4% Gd content. The system undergoes a non-metal to metal transition as suggested by the appearance of filled electron pockets. The device properties resemble those of a tunnel junction diode, which might be related to a band bending at the interface of the film, likely due to surface overoxidation.

Acknowledgement

The outcome of this work has strongly depended upon a collective group of people, who have spent their time and trust on an individual who happens to love what he does. The following list has no order.

To God, for all the events that have led to this day. Thank you…!

To my beloved wife Olha Ketsman, who has been extremely patient and caring during the realization of this work. Thank you so much for your love, understanding and support.

To my father Juan, my sister Sheila and her husband Jose, my aunts Carmen and Maria, my grandpa Juan and my grandmother Carmen and the rest of my family. Thank you for your support from day zero and for always being there for me.

To my group members Yaroslav Ketsman, Lingmei Kong, Xin Zhang, Tao Weng, Shicao, George Peterson and Thomas Scott, who each in their own way has contributed toward my intellectual gain. To Ning Wu for his kindness and good will, for always finding the time to help me no matter how busy he was. To Keisuke Fukutani, for his great support, friendship and all the philosophical conversations that made this journey even more interesting and fruitful.

To my dear friend Shawn Langan, one of the kindest person I have ever met… thank you for all your support troughout these years and thank you for treating me like family.

To my dear friend Thomas A. George, thank you for all your support and the numerous days of Mountain Dew breaks that were accompanied by physics lessons and self-improvement hints so that I could improve my skills every day.

To Dr. Snow Balaz and Catherine Haley for all their help and attentions when I moved in.

To my friend James Glassbrener, a talented scientist who always found the time to entertain my questions, and always managed to answer them in a simple way. Thank you for everything.

To Professor Luis G. Rosa for his encouragement, time and support before and during my graduate studies. Thank you for teaching me so many valuable lessons

To Professor Nicholas Pinto for all of his help and enthusiasm regarding my graduate and undergraduate carriers.

To Professor Claudio Guerra Vela, who inspired me to go beyond by his excellent style of portraying science. You really made a difference!

To Professor Ivelisse Rubio Canabal, who took an infinite amount of her time to provide me with the necesary tools so I could succeed. Thank you so much!

To Yaroslav Lsosovjy, whose great expertise in UHV system, made this work successful, you are the master of the UHV systems… you really are!

To Ihor Ketsman, for all his help and technical support in the laboratory. His devotion to detailed and careful experimentation taught me a lot.

To Professor Carolina Illie, for all her support, kindness and cheerfulness. You always had the right words, thank you for that.

To my Committee Members Profesor Natale Ianno and Professor Eva Schubert for their time invested in this work. Your interest and detailed critique improved my work.

To Jerry L. Hudgins, who have taught me the qualities of a true leader. His kindness, support and time invested in me will be forever appreciated. Thank you for always providing me with the 110%.

And last, but no least, Peter Dowben, from whom if I were to describe his incredible character, another thesis project must be written. Thank you for your unconditional trust and optimism. For extending your lessons beyond those related to science and for teaching me that I can make a difference even when sitting at my desk. Hope the following schematic summarizes your contributions at this stage of my career. Thank you so much for everything!

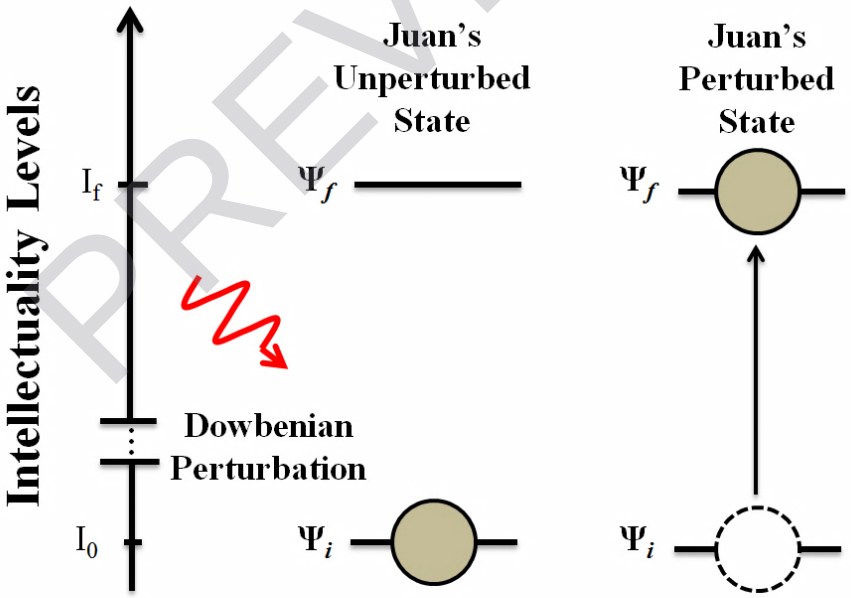

***Note: Ψ_f is known to describe a very stable state

Table of Contents

List of Acronyms iv

List of Figures vi

List of Tables xiii

Chapter 1 Introduction

1.1 Introduction 1

1.1.1 Magnetic Semiconductors 2

References 7

Chapter 2 Experimental Techniques: The Electronic Band Structure

2.1 Photoemission Spectroscopy 10

2.1.1 Photoemission Spectroscopy as an Energy Probe Technique 10

2.1.2 The Photoemission Process 13

2.1.3 Ultraviolet Photoemission Spectroscopy (UPS) 21

2.1.4 X-ray Photoemission Spectroscopy 24

2.1.5 Resonant Photoemission Spectroscopy 22

2.1.6 Matching the Photoemission and the Theoretical Density of States.30

2.1.7 Connection between Photoemission and Reciprocal Space 32

2.1.8 Charging Considerations in PES 36

2.2 Inverse Photoemission Spectroscopy (IPES) 38

2.3 Neutron Detectors 39

2.4 X-ray Absorption Fine Structure 44

References 50

Chapter 3 Sample preparation, Crystallographic Structure and Composition

3.1 Sample Growth Method 53

3.1.1 Hybrid plasma-assisted PVD/CVD process 53

3.1.2 Pulsed Laser Deposition 55

3.2 Crystallographic and Local Structure Studies using X-ray Absorption Fine Structure and X-ray Diffraction 58

3.2.1 The Local Structure of Amorphous Diamond like Carbon doped with Chromium 59

3.2.2 Gadolinium Occupancy in Semiconducting Hafnium Oxide 64

3.2.3 Structural Phase Transition in Gd:HfO_2 66

3.2.4 Comparison of Gd:HfO_2 and Gd_2O_3 Monoclinic Crystal Structure. 67

3.2.5 The (111) Polar Surface in Gd:EuO 68

References 72

Chapter 4 Magnetoresistive Effects in Chromium doped Diamond-like Carbon Heterostructure

4.1 Why Study Chromium doped Diamond-like Carbon? 76

4.2 The Role of Chromium and Chromium Carbide Precipitates 77

4.3 Heterojunctions with Silicon Substrates 82

References 90

Chapter 5 Electronic Band Structure and Transport Caracterization for Magnetic Dilute Semiconductors using High k Dielectric Materials

5.1 A Comparison of Gd_2O_3 and HfO_2: Gd Electronic Band Structure 94

5.1.1 The Experimental and Theoretical Band Structure 94

5.1.2 Heterojunctions using Silicon as a p-type or n-type Substrate 106

5.2 The Effect of Rare Earth Doping (Gd and Ce) in the Electronic Band Structure of EuO Films 108

5.2.1 The Valence Band, Conduction Band and Filling of Electron Pockets 108

5.2.2 Band Bending at the EuO:Gd (111) Polar Surface 117

5.2.3 Magnetic Dependence in Heterojunction Structure 122

References 124

Chapter 6 The Local Metallicity of Gadolinium doped Compound Semiconductors

6.1 Resonant Photoemission as a Probe for Local Metallicity 130

6.2 Resonant Photoemission in EuO films 132

6.3 Comparing the Gd 4d to 4f Photoemission Resonance for Gd in Various Host Semiconductors 138

6.4 Across the Nonmetal to Metal Transition in $Gd_{0.04}Eu_{0.96}O$ 141

References 143

Chapter 7 Gadolinium Based Neutron Detectors

7.1 Why Building Neutron Detectors? 146

7.2 Neutron Detection via Auger Electrons 146

7.3 Single Neutron Capture Detection 149

7.4 Fine Structure in the Neutron Capture Pulse Height Spectra 153

References 158

Chapter 8 Conclusions and Pending Future

8.1 What have we learned? 161

8.2 What is Next? 163

List of Acronyms

ARPES	Angle Resolved Photoemission
BZE	Brillouin Zone Edge
CAMD	Center for Advanced Microstructures & Devices
CB	Conduction Band
CBM	Conduction Band Minimum
CIS	Constant Initial State Spectroscopy
CVD	Chemical Vapor Deposition
DFT	Density Functional Theory
DLC	Diamond-like Carbon
DMO	Dilute Magnetic Oxides
DMS	Dilute Magnetic Semiconductor
DOS	Density of States
EXAFS	Extended x-ray Absorption Fine Structure
FCC	Face Centered Cubic
FM	Ferromagnetic
FL	Fermi Level
FT	Fourier Transform
GMR	Giant Magneto Resistance
IPES	Inverse photoemission Spectroscopy
MBE	Molecular Beam Epitaxy
NIM	Normal Incidence Monochromator
PES	Photoemission Electron Spectroscopy

PLD	Pulsed Laser Deposition
PVD	Physical Vapor Deposition
RPES	Resonant Photoemission Spectroscopy
TGM	Toroidal Grating Monochromator
UHV	Ultra High Vacuum
UPS	Ultraviolet Photoemission
VB	Valence Band
VBM	Valence Band Maximum
VUV	Vacuum Ultraviolet
XAFS	X-ray Absorption Fine Structure
XANE	X-ray Absorption near Edge Structure.
XAS	X-ray Absorption
XPS	X-ray Photoemission
XRD	X-ray Diffraction

List of Figures

Figure 1.1.1 A two-dimensional lattice for (a) an undoped nonmagnetic semiconductor crystal, and a dilute magnetic semiconductor with a random distribution of magnetic dopants ions in the lattice with (b) a paramagnetic behavior and (c) a ferromagnetic coupling due to the introduction of donor defects. The dashed circle represents the Bohr radius of the electron due to the defect …… 2

Figure 1.1.2 Schematic of the physical geometry from which the GMR is observed along with a R vs B plot showing the effect of the magnetic field on the resistance of the structure …… 4

Figure 2.1.1 Schematic of a perturbed system due to an electromagnetic wave from the point of view of energy levels ……..…… 11

Figure 2.1.2 The main elements of the photoemission process. The picture representing the light source is a dual anode x-ray lamp and the detector is a hemispherical angle resolved electron analyzer, both elements are inside a ultra-high vacuum chamber as denoted by the dashed lines …….... 18

Figure 2.1.3 (a) The ultra-high vacuum chamber employed for the PES process at the spectroscopy laboratory in the University of Nebraska and the geometrical set up of the PES elements both (b) into and (c) out of the chamber ……..…….. 20

Figure 2.1.4 Picture of the ultraviolet source employed in our studies. Taken from the Thermo Electron Corporation website ……. 21

Figure 2.1.5 A typical valence band spectra obtain from UPS. The dashed line indicates the secondary electron tail and is due to inelastic scattering of the electrons before reaching the analyzer. Subsequent steps are shown on the top right portion of the figure ……...……...…… 22

Figure 2.1.6 Energy level diagram describing the ultraviolet photoemission process ... 23

Figure 2.1.7 Energy level diagram describing the X-ray photoemission process …...… 24

Figure 2.1.8 (a) The physical geometry of the X-rays source and (b) a schematic of the of the X-ray source. Figure (a) was taken from the Thermo Scientifics application note 31057
…….. 25

Figure 2.1.9 A (a) schematic and (b) picture of the storage ring in CAMD ……... 27

Figure 2.1.10 (a) The 3m TGM beamline and (b) a picture of the TGM ….…….. 28

Figure 2.1.11 (a) The UHV chamber used for the high resolution angle resolved photoemission spectroscopy and (b) the resonant photoemission experiments ……... 29

Figure 2.1.12 The relation between the density of state from a (a) theoretical and (b) experimental point of view. (c) The reference energy between the two DOS distribution 31

Figure 2.1.13 Schematic of the electron propagation along the solid vacuum interface 33

Figure 2.1.14 (a) The first Brillouin zone for a face centered cubic (FCC) lattice and (b) the wavevectors along the direction perpendicular to the surface of a film and the wavevector along the direction parallel to the surface of the film 36

Figure 2.2.1 Energy level diagram summarizing the IPES process 38

Figure 2.2.2 Schematic of the inverse photoemission process 39

Figure 2.3.1. A schematic showing (a) the p-n junction geometry and (b) the depletion region and neutral region of a diode 40

Figure 2.3.2. A p-n junction diode in (a) forward and (b) reverse bias operation 40

Figure 2.3.3 The neutron detection mechanism for a diode detector. The neutrons are incident into a moderator (usually a hydrocarbon plastic) to slow them down. Cadmium foil is used to test for Gamma sensibility although a thin foil of lead is sometime used 42

Figure 2.3.4 Single-chip pulse counting and binning electronics block diagram. The design occupies a total silicon area of 10mm2 fabricated in a 0.35μm CMOS technology (see text). The charge sensitive amplifier (CSA) and analog-to-digital converter (ADC) are indicated schematically 43

Figure 2.4.1 A hypothetical x-ray absorption spectra 45

Figure 2.4.2 Schematic of x-ray absorption in terms of an energy diagram and the absorption probability spectra for the case where (a) there are no neighbors and (b) the photo-electron can scatter from a neighboring atom. 47

Figure 2.4.3 Schematics of experimental setup for XAFS measurement in fluorescence mode from CAMD 48

Figure 3.1.1 Survey of vacuum deposition techniques 54

Figure 3.1.2 (a) Schematic of the pulsed laser deposition process and (b) geometrical set up inside the UHV chamber 56

Figure 3.2.1 The X-ray absorption near-edge structure (XANES) spectra for the Cr-DLC films along with pure Cr and Cr carbide (Cr_3C_2). The spectra are normalized and translated along the *y*-axis (intensity) for clarity 62

Figure 3.2.2 The Fourier transform of the extended X-ray absorption fine structure spectra (EXAFS) for the Cr-DLC films along with pure Cr carbide (Cr_3C_2). The spectra are translated along the *y*-axis (intensity) for clarity 63

Figure 3.2.3 (a) The $k\chi(k)$ of 3% Gd doped HfO_2 extracted from the Gd L_3-edge EXAFS spectra 65

Figure 3.2.4. The Fourier transform (FT) of 3% Gd-doped HfO2 EXAFS data. The oscillating curve (dashed lines) is the imaginary part of the Fourier transform of the data. The envelope (solid lines) are the magnitudes of the Fourier transform. The 3% data are transformed with a square window between 2.8 and 9.4 $Å^{-1}$. The peak assignment is based on HfO_2 65

Figure 3.2.5 Part of the XRD pattern for 3%, 10%, and 15% Gd doped doped HfO_2. The 3% Gd doped films are consistent with that of the HfO_2 in a simple monoclinic structure. The 10% doped samples are mixed monoclinic and majority cubic phases, as indicated, while 15% Gd-doped samples are in a fluorite phase. In the fluorite fcc phase, the lattice constant increases with increased Gd doping 66

Figure 3.2.6 (a) Part of the XRD pattern of the film is shown in figure. X-ray diffraction patterns of PLD grown Gd_2O_3 (upper panel) and 3% Gd doped HfO_2 (lower panel). The bar diagrams included in each panel are the standards of monoclinic Gd_2O_3 and HfO_2, respectively. For 3% Gd doped HfO_2 (lower panel), the XRD is consistent with that of HfO_2 in a simple monoclinic structure. (b) Structure of Gd_2O_3, with the packing of the ions in Gd_2O_3 as viewed along the *b*-axis. The green and red spheres represent gadolinium and oxygen atoms respectively. The Gd .. Gd interactions are not shown 68

Figure 3.2.7 X-ray-diffraction pattern for PLD-grown (a) EuO, (b) Gd-doped EuO films on Si(100) and (c) Ce:EuO 69

Figure 4.2.1 Cr_3C_2 precipitates only at high doping levels, with the precipitates at higher concentration at the interfaces 78

Figure 4.2.2 Photoemission from a 25% chromium doped DLC film (*black*) deposited on silicon, compared to undoped DLC film (*red*). The photon energy was 70 eV and the photoelectrons were collected along the surface normal 79

Figure 4.2.3 The photoemission spectra of the 11.0 % Cr-doped DLC film on silicon as a function of photon energy. The photoelectrons were collected along the surface normal 80

Figure 4.2.4 Hysteresis loops and virgin magnetization curves of Cr-DLC with 3 % Cr at (a) 20 Kelvins and (b) 10 Kelvins 81

Figure 4.3.1 The I –V curves from Cr-DLC films in a heterojunction with n-type silicon, as a function of temperature, for different chromium doping levels (**a**) 5.0 %, (**b**) 11.0 %, (**c**) 15 % and (**d**) 20 % 83

Figure 4.3.2 The I–V curves from the 11 % Cr (**a**) and 15 % Cr (**b**) Cr-DLC film to n-type silicon heterojunction devices with changing applied magnetic field. The change in forward current, as a function of the magnetic field, for Cr-DLC film to n-type silicon heterojunction devices at 11.0 % Cr (**c**), and 15.0 % Cr (**d**). Forward bias voltage was 2.0 V in panels (**c**) and (**d**). All data were acquired at room temperature. In the first trial (*blue*) negative magnetoresistance was observed, but in subsequent trials (*red*) little or no magnetoresistance was found without application of a large field 84

Figure 4.3.3 The I–V curves from a 11 % Cr Cr-DLC film to n-type silicon heterojunction device after magnetization of the sample in a field of 1.0 T. The increase of the negative magnetoresistance is quite evident, and plotted in the *inset* for 2 V forward bias 85

Figure 4.3.4 The resistance of the 11% Cr-doped DLC/silicon heterojunction diode is dependent on voltage in the reverse bias, as indicated in model calculations. The forward bias does not have the same dependence, because the function $R(H)$ is constant with $V > 0$. The schematic is the ideal of the effective circuit for the model calculations 86

Figure 4.3.5 In the forward bias, in simple model calculations, the resistance of the 11% Cr-doped DLC/silicon heterojunction diode decreases as the applied magnetic field increases 89

Figure 5.1.1 Different bands intensities for pristine and Gd-doped films of HfO_2. The photon energy used was 100 eV and the light incidence angle is 45°. All photoelectrons were collected along the surface normal at T = 320 °C 95

Figure 5.1.2 The photoemission spectrum of the valence band Gd_2O_3 $< \bar{4}02 >$. The various components contributing to the valence band structure are indicated and major contributions to the photoemission features indicated. The photon energy is 117 eV and the light incidence angle is 45°. All photoelectrons were collected along the surface normal at T = 240 °C 96

Figure 5.1.3 Resonant photoemission spectra for photon energies through the 4d → 4f resonance for Gd doped films of HfO_2. Light incidence angle is 45°. All photoelectrons were collected along the surface normal 97

Figure 5.1.4 The resonant photoemission spectra for photon energies through the 4d → 4f resonance for Gd_2O_3. Light incidence angle is 45◦. All photoelectrons were collected along the surface normal 98

Figure 5.1.5 The resonant photoemission intensities through the 4d→ 4f resonance for Gd_2O_3 (a) and Gd doped films of HfO_2 (b). ForGd_2O_3, there are seen to be two Gd 4f components at a binding energy of about 8.7–9.5 eV below the Fermi level and the 'shoulder' at a binding energy of 11–12 eV, which are assigned as bulk (*black*) and surface (*red*) components respectively ……..…...…. 99

Figure 5.1.6. The calculated density of states for monoclinic (type B) Gd_2O_3. The monoclinic Gd_2O_3 density of states (DOS) has been broadened with a Gaussian width 0.2 eV. The total density of states has been projected onto each atomic species (gadolinium and oxygen) showing the strong Gd 4f character at the DOS peak around E =-6.3 eV and the major oxygen 2p character hybridized with Gd 5d orbitals over the energy range of −5 to 0 eV …….. 102

Figure 5.1.7 The dispersion of the Gd 4f component, with changing photon energy. The critical points are indicated, assuming no inner potential and the predicted lattice spacing of 23.7 Å along $< \bar{4}02 >$ ……..……. 104

Figure 5.1.8 A heterojunction diode constructed from Gd-doped HfO_2 on silicon, for various Gd-doping concentrations. With oxygen vacancies, the Gd doping generated acceptor states, in 3% Gd-doped HfO_2, are over compensated and doped hafnium oxide forms a rectifying diode on *p*-type silicon (a). The 10% Gd-doped HfO_2 is not overcompensated by oxygen vacancies and does not form a rectifying diode on *p*type silicon (b) but does do so on *n*-type silicon (c) ……..……. 107

Figure 5.2.1. The simulated (solid line) and experimental (dashed line) photoemission spectra for undoped EuO, with corrections for the combined excited-state density of states. The DFT/GGA calculations of density of states (DOS) were performed with fixed occupancies for treating the excited states ……..…… 109

Figure 5.2.2 Combined ARPES and IPES spectra for (a) undoped EuO film, (b) $Eu_{0.96}Gd_{0.04}O$ (111) film, and (c) same as (b) but after sputtering. A photon energy of 60 eV was used, with light incident at 45° and photoelectrons collected along the surface normal. For the IPES spectra the electrons are incident along the surface normal ….. 113

Figure 5.2.3 The photoemission spectra obtained for $Eu_{0.96}Gd_{0.04}O$ (111) films as a function of the photon energy. The angle of incidence was 45° and all photoelectrons were collected along the surface normal at T = 300 K ……..…. 115

Figure 5.2.4 (a) The Fermi level intensity (*blue*) plotted as a function of $k_\perp$, along the [111] direction. (b) The dispersion of the Eu 4*f* weighted band at the valence-band maximum, along the (111) direction or wave vector normal to the surface, $k_\perp$. Both results were extracted from the photon energy dependent ARPES spectra. BZE indicates the Brillouin-zone edge. The intensity of the Eu 4*f* weighted band (+), at the valence-band maximum, along the $k_\perp$ (111) direction, is also plotted in (a) ……...… 115

Figure 5.2.5 The Fermi-level intensity plotted as a function of the parallel momentum $k_{||}$ along the ΓM direction, for photon energies of (a) 40 eV and (b) 25 eV. For $k_{||}$ along the ΓM direction, the relative intensity has been also plotted 300–400 meV below the Fermi level (green) and at the Fermi level (red), to illustrate the roughly parabolic shape of the electron pocket about the surface Brillouin-zone edge at 40 eV ……..…..... 117

Figure 5.2.6 Calculated structure of the O-terminated EuO(111) surface. Only half of the slab is shown, the other half being symmetric. For interlayer spacings see Table 5.2.1. In the figure, large spheres are Eu atoms; small spheres: O atoms…… 120

Figure 5.2.7 Site-projected DOS for all Eu and O atoms of the 27-monolayer slab of Gd-doped-EuO with (111) surfaces. A model with empirical adjustments is used (see text). (a) Eu site-projected DOS where the unoccupied DOS is multiplied by 5 (as indicated). (b) O site-projected DOS; unoccupied DOS is multiplied by 10 (as indicated). The numbering of the sites starts at the surface ……...……. 121

Figure 5.2.8 *I-V* curves for (a) undoped EuO(100) film as a function of temperature, (b) $Eu_{0.96}Gd_{0.04}O$ (111) film at room temperature. The curve marked (*i*) is for zero field; the curve marked (*ii*) is for an external magnetic field of 1000 Oe ……..... 123

Figure 6.2.1 Valence band spectra obtained from the photoemission density of state for (a) EuO and (b) $Eu_{0.96}Gd_{0.04}O$ films grown on p-type Si (100). The composition of the spectra was determine by the Gaussian distributions and the photoemission feature were classified as arising from largely the (A) Eu $4d_{5/2}$ and electron pockets of the conduction band minimum, (B) Eu $4d_{3/2}$ (C) O 2s, (D) O 2s and (E) Gd 4f and Eu 4f final state (satellite) contributions. Photoelectrons were collected along the surface normal. Measurements for both films were taken using synchrotron light with photon energy of 60 eV and incidence angle of 45°. Binding energy is denoted in terms of $E\text{-}E_F$ …...… 133

Figure 6.2.2 (a) The photoemission spectra for photon energies through the Gd and Eu 4d to 4f super koster Kronig photoemission resonance for $Eu_{0.96}Gd_{0.04}O$ films. (b) The resonant photoemission intensities, as a function of photon energy i.e. constant initial state spectra, for the valence feature at (i) 0.5 eV, (ii) 2.3 eV, (iii) 6.1 eV and (iv) 9.2 eV below the Fermi level. Light was incident at 45°. Photoelectrons were collected along the surface normal. Binding energy is denoted in terms of $E\text{-}E_F$ ……...… 135

Figure 6.3.1 Valence band photoemission spectra "on" (photon energy of 147 eV) and "off" (photon energy of "off" with hν= 140, 139.7 and 132 eV for $Eu_{0.96}Gd_{0.04}O$, $Gd_{0.03}Ga_{0.97}N$, $Gd_{0.03}Hf_{0.97}O_2$ respectively) the Gd 4d to 4f resonant photoemission feature obtained for (a) $Eu_{0.96}Gd_{0.04}O$, (b) $Gd_{0.03}Ga_{0.97}N$ and (c) $Gd_{0.03}Hf_{0.97}O_2$. All photoelectrons were collected along the normal to the film surface. Binding energy is denoted in terms of $E\text{-}E_F$ …… 139

Figure 6.3.2 Constant initial state valence intensity as a function of photon energy in the region of Gd 4f contributions to the valence band (-9 eV binding energy, $E\text{-}E_F$.) in Gd doped (a) GaN (3%), (b) HfO_2 (3%) and (c) EuO (4%) host systems …….... 141

Figure 6.4.1 Resonant photoemission intensity as a function of photon energy for the Eu 4f weighted features in the valence band at about -2 eV binding energy ($E-E_F$) in (a) EuO and (b) $Eu_{0.96}Gd_{0.04}O$ films. The decrease in intensity suggests a major change in metallicity with the inclusion of 4% percent Gd 141

Figure 7.2.1. A summary of the major decay routes for ^{158}Gd in the excited state through emission of high energy gamma rays, low-energy gamma rays, x-rays, internal (IC) and Auger Coster–Kronig (ACK) conversion electrons as $^{157}Gd(n,\gamma) \rightarrow 158\ Gd + \gamma +$ x-rays + IC e^- + ACK e^- 148

Figure 7.3.1 A heterojunction diodes constructed from $Hf_{0.85}Gd_{0.15}O_{1.92}$ on n-type silicon. The $Hf_{0.85}Gd_{0.15}O_{1.92}$ is not overcompensated by oxygen vacancies and does not form a rectifying diode on p-type silicon but does do so on n-type silicon 150

Figure 7.3.2 Pulse height spectra obtained using $Hf_{1-x}Gd_x\ O_{2-0.5x}$ combined contributions of Gd–O, and Gd–Hf single-scattering paths as well as several multiple-scattering (+MS) paths 151

Figure 7.3.3. The pulse height spectra of $Hf_{0.85}Gd_{0.15}O_{1.92}$ on n-type Si(100) samples with thermalized neutrons from a PuBe source with a flux of 600 neutrons s^{-1} incident on the diode, compared with an MCNP 5.0 simulation, modified to account for suppression of the pulses of pulse height less than 200 mV in experiment 152

Figure 7.4.1. A sampling of a time domain pulse height spectra using $Hf_{0.85}\ Gd_{0.15}\ O_{1.92}$ on n-type Si(100) samples irradiated with thermalized neutron from a PuBe with a flux of 600 neutrons $cm^{-2}\ s^{-1}$. The offset of the baseline from 0 V is not meaningful, and a consequence of the display routine 156

List of Tables

Table 3.2.1 Structural parameters for Cr-DLCs and Cr_3C_2 obtained from curve fitting Sample Model fit ……..…… 64

Table 5.2.1 The interlayer spacing calculated for EuO(111) as indicated in Figure 5.2.6. The layer spacings are oscillatory in the region of the surface, as indicated. The layers spacing are giving in units of Å ……..……..……...….. 120

Table 6.3.1. Summary the photon energy for resonant photoemission intensity maximum, the width of the Gd 4d to 4f photoemission resonance, in photon energy and the intensity ration of "on" resonance at a photon energy of 147 eV to the "off" resonant intensity at a photon energy of eV ……..…. 140

Chapter 1 Introduction

This thesis explores how the inclusion of a small percent of magnetic impurity affects the magnetization properties and electronic band structure of a set of different host semiconducting compound materials. Much of the emphasis will be on gadolinium which we employed, both as a dopant and as a member of the compound itself, given its valuable intrinsic properties (particularly the large magnetic moment of 7.3 μ_B per atom). Key questions towards the ensemble of this work are: Can we make heterojunction devices out of these materials? If we do fabricate devices, do they exhibit magnetic dependence? What is the role of gadolinium in highly correlated semiconductor systems, given the large on-site energy due to the half-filled 4f orbital ($4f^7$).

In fact addressing the latest question is quite complex. Gadolinium is usually treated as having a stable 3+ valence state when inserted into host semiconductors. The electrons in the 4f orbitals remain fairly localized to the ion vicinity, likely due to the partial screening provided from the outermost closed subshells. This leads to the situation in which the electrons with the lowest energy does not correspond to the outermost shell of the atom, but a shell located underneath, hence, the 4f electron are somewhat restricted from interacting directly with the neighbor atoms surrounding the ion. Yet, we found that the effect of increasing the gadolinium concentration is very different in each particular semiconductor. In most cases, the 4f electrons form part of the valence band and directly contribute to strong hybridization between the ion and neighboring atoms.

Nonetheless, before diving into the complexity of these issues, let's not deviate from our major goal (i.e. devices with magnetic properties). On this behalf, let's point out the road that led to the foundations of this work from a historical point of view.

1.1 Magnetic Semiconductors

A magnetic semiconductor is a material that exhibit both, ferromagnetic behavior and semiconducting properties simultaneously. Ferromagnetism refers to a material with the ability to remain magnetized after the application of an external magnetic field and a semiconductor is a material with a small electronic band gap and the ability to partly conduce current. In contrast, a dilute magnetic semiconductor (DMS) refers to the same type of material with the difference that is doped with atoms that possess an intrinsic magnetic moment (such as Gd). The idea behind these devices relies on increasing the Curie temperatures of our compounds via the interaction of magnetic impurities and free carriers form via defect in the compound structure as shown in Figure 1.1.1.

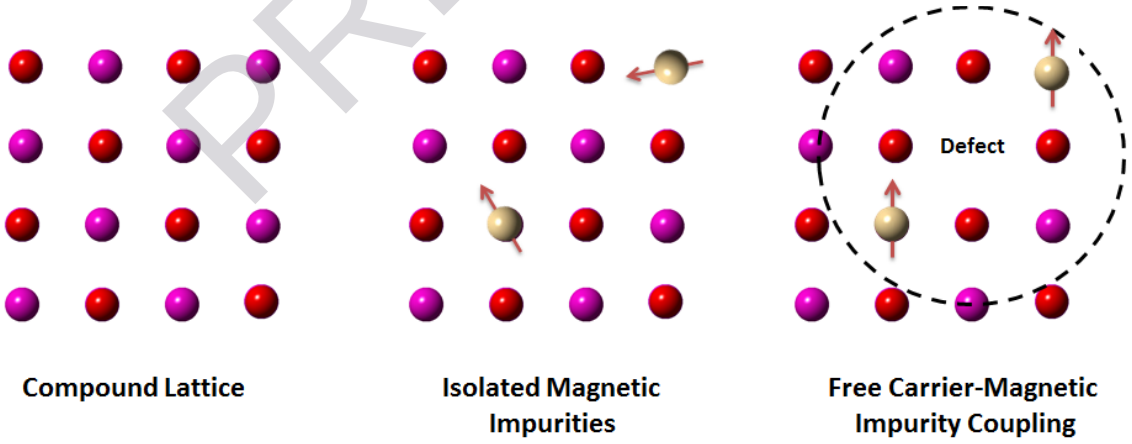

Figure 1.1.1 A two-dimensional lattice for (a) an undoped nonmagnetic semiconductor crystal, and a dilute magnetic semiconductor with a random distribution of magnetic dopants ions in the lattice with (b) a paramagnetic behavior and (c) a ferromagnetic coupling due to the introduction of donor defects. The dashed circle represents the Bohr radius of the electron due to the defect.

As simple as the concept behind DMS materials sounds, it turns out that the physics of these materials is fairly complex. To understand their true value we must gain insight on the importance of DMSs. To this end, a brief history of spintronics research must be reviewed. The portmanteau "spintronics" is a combination of both spin (an intrinsic property of electrons) and electronics (field concerned with circuitry design). The name fits quite well to this technology as it exploits the spin of the electron in addition to the electron charge as seen in conventional devices such as diodes and transistors. In 2007, Albert Fert and Peter Grùnberg won the Nobel Prize in physics for their independent work in the discovery of the giant magnetoresistance (GMR) back in 1988 [1, 2], an event which some considered as the birth of spintronics. The GMR effect is observed when two metallic ferromagnetic layers are separated by a nonmagnetic material (usually a few nm thick). Depending on the net magnetization of the two ferromagnetic materials the electrical resistance will change as shown in Figure 1.1.2. For parallel alignment the resistance is low whether for antiparallel alignment the resistance is high.

This phenomenon has led to applications such as read heads for modern hard drives, magnetic sensors and tunnel magnetoresistance. There are several reviews of GMR [3] and spintronics applications [4-6] available, with a more detailed description of this field and the application mentioned above. For the purpose of this work it suffice to understand that a magnetic field can influence the resistance of a material, and hence the current through it.

Unfortunately, there is a downside with all the applications mentioned above as their implementation is limited to the use of ferromagnetic metals. Ferromagnetic materials are not susceptible to an applied electric field, resulting in difficulties if one

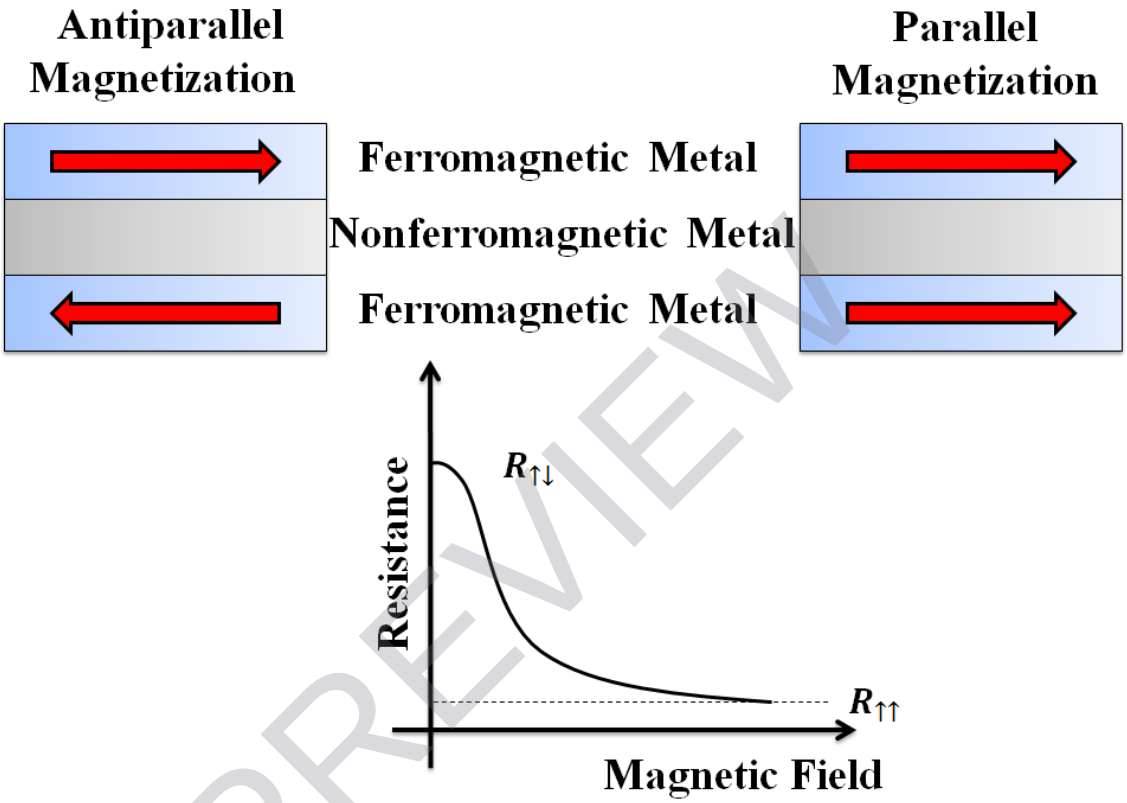

Figure 1.1.2 Schematic of the physical geometry from which the GMR is observed along with a R vs B plot showing the effect of the magnetic field on the resistance of the device structure.

wants to exploit the charge of the carrier. Semiconductor materials are much more sensitive to electric field dependence [7] and are indeed one of the reasons for many dilute magnetic semiconductor (DMS) studies. Imagine a world in which you can merge the current semiconducting technology with magnetism (memory) in a single material… great things will come from it! The first DMS studies were performed in the late 70's

and were heavily considered in the 80's. Among these, II-IV and III-V based DMSs such as (Zn, Mn)Se and (Ga, Mn)As were popular. Special efforts were invested in (Ga, Mn)As [8] and (In, Mn)As [9] as ferromagnetic order was achieved by Hideo Ohno's and co-workers with a Curie temperature of 140 K at the time [8], although T_C of 180 K were later achieved by careful growth of the material. In 2000, Dietl's [10] came up with a model (based on that by Zener [11]) to explain the ferromagnetic behavior in these materials and triggered a search for room temperature magnetism. This model does provide good insights in the description of the experimental data, but some fundamental aspects of these complex materials are still controversial. There is still an ongoing debate as whether or not one can identify an impurity band in materials with high T_c and whether the charge transport and magnetic interaction are mediated by localized or extended states, as these states are close to the Fermi level. High doping concentrations result in a wider impurity band and can lead to a mixing with the valence band [12].

There is another type of potential ferromagnetic semiconductor material, the dilute magnetic oxides (DMOs) which are more pertinent to this work. Perhaps, the most popular model today is that proposed by Coey [13] in which ferromagnetic exchange is mediated by shallow donor electrons that form bound magnetic polarons. If overlap of these occurs, a spin-split impurity band can be created. Since the carriers are expected to couple strongly to the magnetic moments, DMOs might be a route for interesting spintronics applications. Ferromagnetism above room temperature has been reported, but the results are irreproducible and observed only in non-crystal films (and bulk material), in which case, the effects can be attributable to magnetic secondary phases. This opens up